Crystal structure and electrical and optical properties of two-dimensional group-IV monochalcogenides

Mateus B. P. Querne,[1] Jean M. Bracht,[1] Juarez L. F. Da Silva,[2] Anderson Janotti,[3] and Matheus P. Lima[1,*]

[1]*Department of Physics, Federal University of São Carlos, 13565-905 São Carlos, São Paulo, Brazil*

[2]*São Carlos Institute of Chemistry, University of São Paulo, P.O. Box 780, 13560-970 São Carlos, São Paulo, Brazil*

[3]*Department of Materials Science and Engineering, University of Delaware, Newark, Delaware 19716, USA*

(Received 30 March 2023; revised 17 June 2023; accepted 20 July 2023; published 7 August 2023)

Two-dimensional (2D) semiconductor materials offer a platform for unconventional applications such as valleytronics, flexible nanoelectronics, and hosts of quantum emitters. Many of these materials and their electronic properties remain to be explored. Using *ab initio* simulations based on the density functional theory, we investigate group-IV monochalcogenides MQ (M = Si, Ge, Sn and Q = S, Se, Te), an emerging class of 2D materials, with two competing crystal structures: (i) phosphorenelike ($Pmn2_1$), which has already been synthesized, and (ii) SiTe-type ($P\bar{3}m1$), which has been much less explored. Except for SnS, we find that the SiTe type is the lowest-energy structure and has higher structural stability, motivating efforts to synthesize this less explored $P\bar{3}m1$ phase. Regarding the optoelectronic properties of these two phases, in the $P\bar{3}m1$ phase, MQ compounds have band gaps around the sunlight spectrum peak and show narrower variations in band gap with the composition and higher absorption coefficients for lighter chalcogens. In contrast, in the $Pmn2_1$ phase, MQ compounds have wider band gaps and show a band gap variation of up to 72% with composition, higher absorption coefficients with Te atoms, and potential for valleytronics. In particular, SiS shows interesting high optical anisotropy among all the investigated materials. Furthermore, the optical spectra present peaks that are particular to each phase or composition, making the refractive index a distinguishing parameter for identifying the different MQ compounds. Finally, a phase transition from monolayer to bulk due to an interaction between the layers is observed. Thus, the present results straighten out the role of the crystalline phase in the optoelectronic properties of these monochalcogenides.

DOI: 10.1103/PhysRevB.108.085409

I. INTRODUCTION

Two-dimensional materials have attracted significant interest in the last decade due to their unique properties such as a high degree of anisotropy [1,2] and chemical functionality over relatively large areas [3]. Since the graphene breakthrough [4,5], a wide variety of two-dimensional (2D) materials have been predicted [6,7] and experimentally characterized [8–10], with the most prominent family being transition-metal dichalcogenides [11–15], namely, MoS_2, $MoSe_2$, WSe_2, WTe_2, etc., encompassing semiconductors [16], topological semimetals [17], etc. These unconventional materials with diverse properties create opportunities for many applications, from nanoelectronics [18] to photovoltaics [19] and biomedicine [20].

In the past few years, a new class of 2D materials came to prominence because of their chemical flexibility and variations in crystal structures [21]. These layered materials have formula units consisting of one atom from group IV (M) of the periodic table, and one chalcogen (Q) and are called group-IV monochalcogenides, represented by the chemical formula MQ. Recent theoretical and experimental works considered MQ in orthorhombic structures that resemble that of black phosphorus [22–25], named here phosphorenelike (Ph-like) structures (see Fig. 1, right), leaving aside other possible 2D structures that could be more stable than the Ph-like structure and have distinct properties.

A few theoretical works have explored the MQ materials within the $P\bar{3}m1$ space group [26] (see Fig. 1, left), finding interesting properties such as nontrivial band gaps, pressure-induced topological transitions [27], and strain-tunable optoelectronic properties [28]. Despite the absence of experimental evidence of freestanding $P\bar{3}m1$ monolayers to date, the SiTe monolayer is part of the already synthesized three-dimensional $(SiTe)_2(Sb_2Te_3)_n$ structure [29], paving the way for the isolation of a $P\bar{3}m1$ (SiTe-type) monolayer through the "Scotch-tape" method. A systematic comparison of MQ compounds in Ph-like and SiTe-type structures is still lacking in the literature.

In this work, we contrast the properties of MQ compounds in Ph-like and SiTe-type structures via *ab initio* simulations based on the density functional theory (DFT) [30,31]. We consider nine MQ compounds based on elements in group IV (M = Si, Ge, Sn and chalcogens Q = S, Se, Te). The already synthesized SnS compound [22] is the only one with lowest energy in the Ph-like phase, whereas the two phases are equally energetically favorable in the case of SnSe; all the other compounds in the MQ family are more energetically favorable in the less explored SiTe-type phase.

We find from phonon dispersion calculations that the MQ compounds are stable in the SiTe-type structure, whereas

*mplima@df.ufscar.br

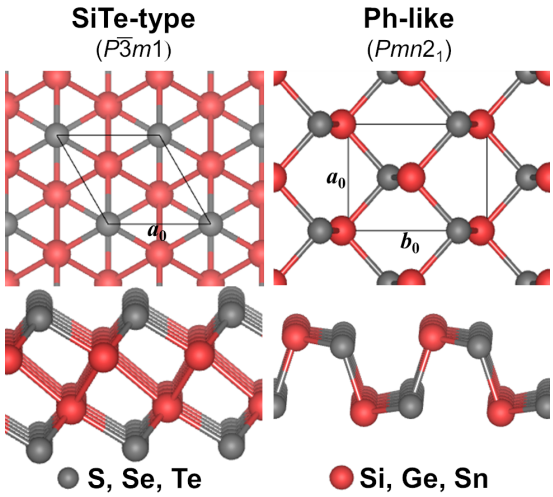

FIG. 1. Ball and stick representations of the SiTe-type structure (left), space group $P\bar{3}m1$, and Ph-like structure (right), space group $Pmn2_1$, of the 2D MQ compounds investigated.

negative frequencies near the Γ point are predicted for the MQ compounds in the Ph-like structure. Peaks in the optical spectra indicate better sunlight absorption in SiTe-type MQ compounds with lighter chalcogens. For the electronic properties, the band gaps of Ph-like MQ compounds change more drastically with chalcogen species (S → Se → Te), with a variation of 72%. The MQ compounds in the Ph-like structure, SiS in particular, also show pronounced anisotropy in their electronic structure, with different valleys along the Γ-X and Γ-Y directions. We propose the use of the refraction index as a way to identify the MQ compounds in these two different phases. Finally, we show a phase transition from the monolayer to the bulk measured through the calculation of the formation enthalpy and the energy decomposition that indicates an interaction between the layers, which is confirmed by deformation energy in the range of 0.06–0.11 and 7.43–14.82 meV/Å^2 for the SiTe-type and Ph-like structures, respectively, along with the characterization of the interlayer binding mechanisms via spatially resolved charge density analysis for both phases that revealed the concentration of charge only in the interlayer region of the Ph-like structure.

II. METHODOLOGY

Version 5.4.4 of the Vienna *Ab initio* Simulation Package (VASP) [32] was used to obtain the results of the DFT calculations [30,31]; the method chosen to solve the Kohn-Sham equation was the projector augmented-wave (PAW) method [33]. The exchange-correlation functional proposed by Perdew, Burke, and Ernzerhof (PBE) [34] was adopted for the optimization of the atomic positions and lattice parameters; however, the screened hybrid functional proposed by Heyed, Scuseria, and Ernzerhof (HSE06) [35] was employed to improve the description of the electronic properties, e.g., band gaps. We calculated the optical properties from the evaluation of the dielectric function in the linear response regime as detailed by Gajdoš *et al.* [36] in the PBE framework, but correcting the band gap using a "scissors operator" [37] based on the HSE06 calculations, (i.e., we blueshifted the absorption coefficient according to the differences in the HSE06 and PBE calculated band gaps). From our own computational test calculations, which are shown in the Supplemental Material [38], we found that spin-orbit coupling does not play a relevant role in the electronic structure of the studied materials.

Stress-tensor calculations allow the relaxation of atomic positions and lattice parameters using the conjugate gradient method until the forces on all atoms are smaller than 0.01 eV/Å. For these calculations, we expanded the Kohn-Sham (KS) wave functions with plane waves truncated with cutoff kinetic energies of 517 eV for SiS and GeS; 491 eV for SiSe and SiTe; 423 eV for GeSe; 350 eV for GeTe; and 520 eV for SnS, SnSe, and SnTe, which are twice the maximum values recommended by the PAW projectors. However, we calculated the remaining properties by freezing the already optimized structure while expanding the KS orbitals in a plane-wave basis set with a cutoff kinetic energy 12.5% higher than the maximum value recommended by the PAW projectors, i.e., 291 eV for SiS and GeS; 276 eV for SiSe and SiTe; 238 eV for GeSe; 197 eV for GeTe; and 292 eV for SnS, SnSe, and SnTe. These values take into account the slower convergence of stress tensors compared to electronic properties when considering the cutoff kinetic energy. The convergence criterion for total energy is set to 1×10^{-6} eV. A length of $R_{\mathbf{k}} = 35$ Å defines Γ-centered **k**-mesh samplings of $Nk_x \times Nk_y \times 1$, where Nk_i ($i = x, y$) represents the next integer to $R_{\mathbf{k}} b_i$, with b_i being the modulus of the reciprocal lattice vector. This equation results in a **k** grid of $10 \times 10 \times 1$ for SiTe-type SiS (the remaining parameters are shown in the Supplemental Material [38]). Moreover, we used a vacuum thickness of 15 Å between the periodic images of the monolayers to avoid spurious interactions between them. Further details of the calculations are contained in the Supplemental Material [38].

The phonon band structures were obtained using the PHONOPY code [39,40] based on VASP calculations. Supercells of dimensions $2 \times 2 \times 1$, $3 \times 3 \times 1$, and $4 \times 4 \times 1$ were considered in these calculations in order to attest the stability of the materials. For the optical absorption coefficients we set the complex shift of the Kramers-Kronig transformation to 0.05 eV. The VASPKIT tool [41] was used for the postprocessing of the optical absorption data.

III. RESULTS AND DISCUSSION

A. Structural parameters

Figure 1 shows ball and stick model representations of the investigated monochalcogenides. The SiTe-type structure has a core region of group-IV atoms with a buckled hexagonal structure (similar to silicene [42]) between two triangular lattices of chalcogens. The Ph-like structure has an orthorhombic unit cell with two puckered layers stacked together. Here, each M (Q) atom is coordinated to three Q (M) atoms with an sp^3 hybridization. The shortest lattice parameter (a_0) points in the MQ zigzag direction, whereas the longest one (b_0) is perpendicular to the trenches. This peculiar bonding geometry leads to anisotropic effects like those already found in analogous materials [43]. The ratio b_0/a_0 is a measure of the

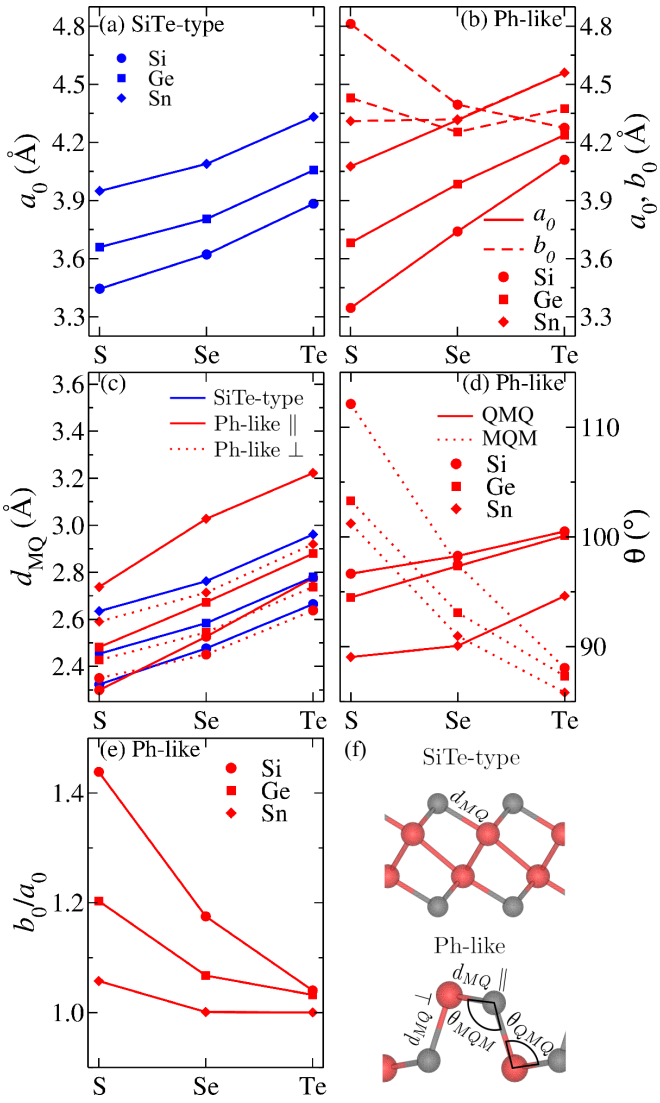

FIG. 2. Structural parameters for the group-IV monochalcogenides MQ: (a) lattice parameter a_0 for SiTe-type structures, (b) lattice parameters a_0 and b_0 for Ph-like structures, (c) MQ bond lengths d_{MQ} for SiTe-type and Ph-like structures, (d) internal angles θ for Ph-like structures, (e) lattice anisotropy (b_0/a_0), and (f) MQ bond lengths and internal angles.

lattice anisotropy, and it can change with the composition for similar materials [44].

Aiming to assist with future experimental characterization [45] of these materials, we calculated the structural parameters of the MQ compounds. Figure 2 shows the basic parameters of MQ in the SiTe-type and Ph-like structures. The lattice parameter a_0 of the SiTe-type structures monotonically increases with the atomic number of M and Q atoms, as shown in Fig. 2(a). The distance between M and Q (d_{MQ}) follows the same trend as the lattice parameter, as seen in Fig. 2(c). We attribute this monotonic relation between the bond lengths and the lattice parameters to the atomic radii [46]. The internal structural parameters, such as angles and layer thickness, do not change this relation.

The Ph-like structures also present a monotonic behavior for a_0 and MQ bond lengths. However, this behavior is not observed for b_0, as shown in Fig. 2(b). An analysis of the internal parameters is needed to understand this result. As shown in Fig. 2(f), there are two MQ bond lengths, namely, $d_{MQ}\perp$ and $d_{MQ}\parallel$, and two internal angles, namely, θ_{MQM} and θ_{QMQ}. Despite the nonmonotonic behavior of b_0, all bond lengths increase with atomic radii [46]. Furthermore, $d_{MQ}\parallel$ for the Ph-like structures are close to d_{MQ} for the SiTe type, as in Fig. 2(c). The nonmonotonic behavior of b_0 can be attributed to changes in the θ_{MQM} and θ_{QMQ} parameters, causing variations in the trenches' widths and depths. While θ_{QMQ} increases with the atomic radii at a small rate, θ_{MQM} decreases with the radii at a larger rate, resulting in a narrowing of the trenches and hence in a tendency to reduce b_0, as shown in Fig. 2(d). Thus, b_0 decreases due to angular variations, and it tends to increase due to atomic radii, which are the two competing parameters that give the nonmonotonic behavior of b_0 for the Ph-like structure. The angular variations do not affect a_0 as it is in the zigzag direction, ruled mostly by $d_{MQ}\parallel$. The anisotropy parameter b_0/a_0 has higher (lower) values for lighter (heavier) materials, as shown in Fig. 2(e). Interestingly, b_0/a_0 is close to 1 for the Te-based materials, leading to a quasitetragonal phase.

TABLE I. Structural parameters of some MQ compounds and, in parentheses, their reported values in the literature.

MQ	Phase	a_0 (Å)	b_0 (Å)
SiSe [47]	SiTe type	3.62 (3.62)	
SiTe [26]	SiTe type	3.88 (3.99)	
GeSe [47]	SiTe type	3.80 (3.81)	
GeTe [47]	SiTe type	4.06 (4.06)	
SnTe [27]	SiTe type	4.33 (4.29)	
GeS [48]	Ph-like	3.68 (3.67)	4.43 (4.39)
GeSe [48]	Ph-like	3.98 (3.92)	4.25 (4.30)
SnS [49]	Ph-like	4.08 (4.07)	4.31 (4.24)
SnSe [49]	Ph-like	4.31 (4.30)	4.31 (4.36)

There are limited experimental and theoretical results in the literature for some of the MQ materials investigated here. Table I shows the structural parameters calculated by us in comparison to reported values in the literature. Thus, our calculated lattice parameters are in good agreement with available experimental and calculated values.

B. Stability

In this section, we discuss the stability of the MQ materials through their formation enthalpy ΔH (energetic stability) and phonon dispersion (vibrational stability).

1. Energetic stability

Herein, to access the energetic stability, we calculate the formation enthalpy per formula unit ΔH [50] using the following equation:

$$\Delta H = (E_{\text{tot}} - n_M\mu_M - n_Q\mu_Q)/N\,, \tag{1}$$

where N is the number of formula units in the unit cell; E_{tot} is the total energy of the investigated monolayer; $n_{M(Q)}$ is the number of group-IV (chalcogen) atoms in the unit cell; and $\mu_{M(Q)}$ is the elemental chemical potential, calculated as the total energy per atom for the lowest-energy elemental bulk

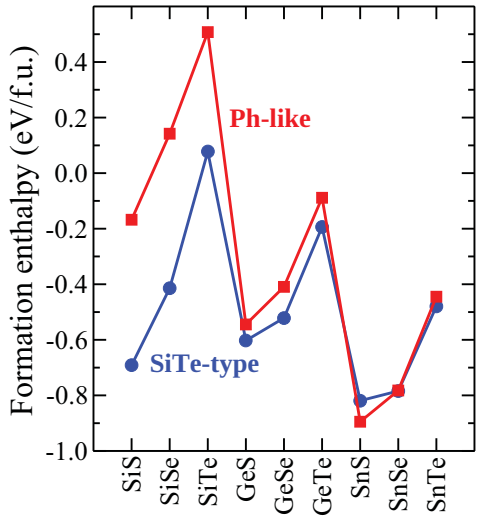

FIG. 3. Calculated formation enthalpies for group-IV monochalcogenides in the SiTe-type and Ph-like structures.

structures, i.e., diamondlike cells for group-IV elements, a trigonal structure with space group $R\bar{3}$ for S, and trigonal $P3_121$ structures for both Se and Te. The results are shown in Fig. 3.

The SiTe-type structures have the lowest formation enthalpy for all compounds, except for the SnS compound, for which the Ph-like structure is lower by 9.1%, while for the SnSe compound, the formation enthalpies differ by only 2 meV. These results indicate that monolayers experimentally synthesized in the Ph-like structure, such as GeS, GeSe, and SnSe [22,51,52], have the lowest-energy counterparts in the SiTe-type structure.

There are three endothermic ($\Delta H > 0$) compounds, namely, SiSe and SiTe in the Ph-like structure and SiTe in the SiTe-type structure, which are energetically unstable materials in freestanding form. Their stabilization depends on nonequilibrium mechanisms such as the use of a substrate [53]. The other 15 compounds are exothermic ($\Delta H < 0$); thus, they are energetically stable. The formation enthalpy decreases with the atomic radii of the Q atoms except for the SiTe-type compounds SiS and GeS, while it increases for all compounds with atomic radii of the M atoms. This is attributed to the difference in electronegativity between M and Q, in which the more stable the compounds are, the more ionic their chemical bonds are [54]. Our results for the energetic stability of MQ compounds motivate the experimental search for routes for the growth of the monochalcogenide monolayer with SiTe-type structure.

2. *Vibrational stability*

The phonon band structures for the MQ compounds are shown in Fig. 4. As all primitive cells have four atoms, there are 12 phonon branches (3 acoustic and 9 optical), in which the 3 acoustic branches coexist with 3 optical branches in the same (low-frequency) region, revealing the possibility of

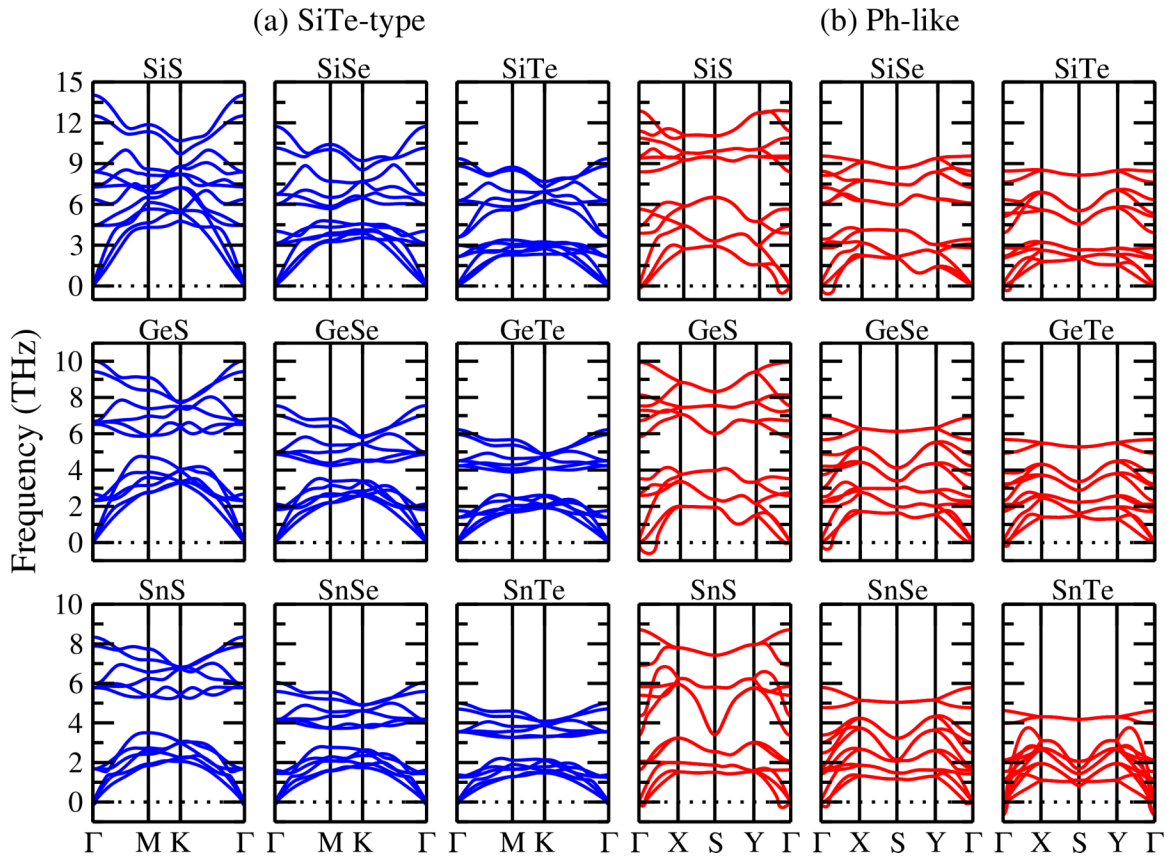

FIG. 4. Calculated phonon dispersions (using the GGA-PBE functional) for group-IV monochalcogenides in (a) the SiTe-type and (b) Ph-like structures. The dotted lines at zero indicate the real/imaginary frequency threshold.

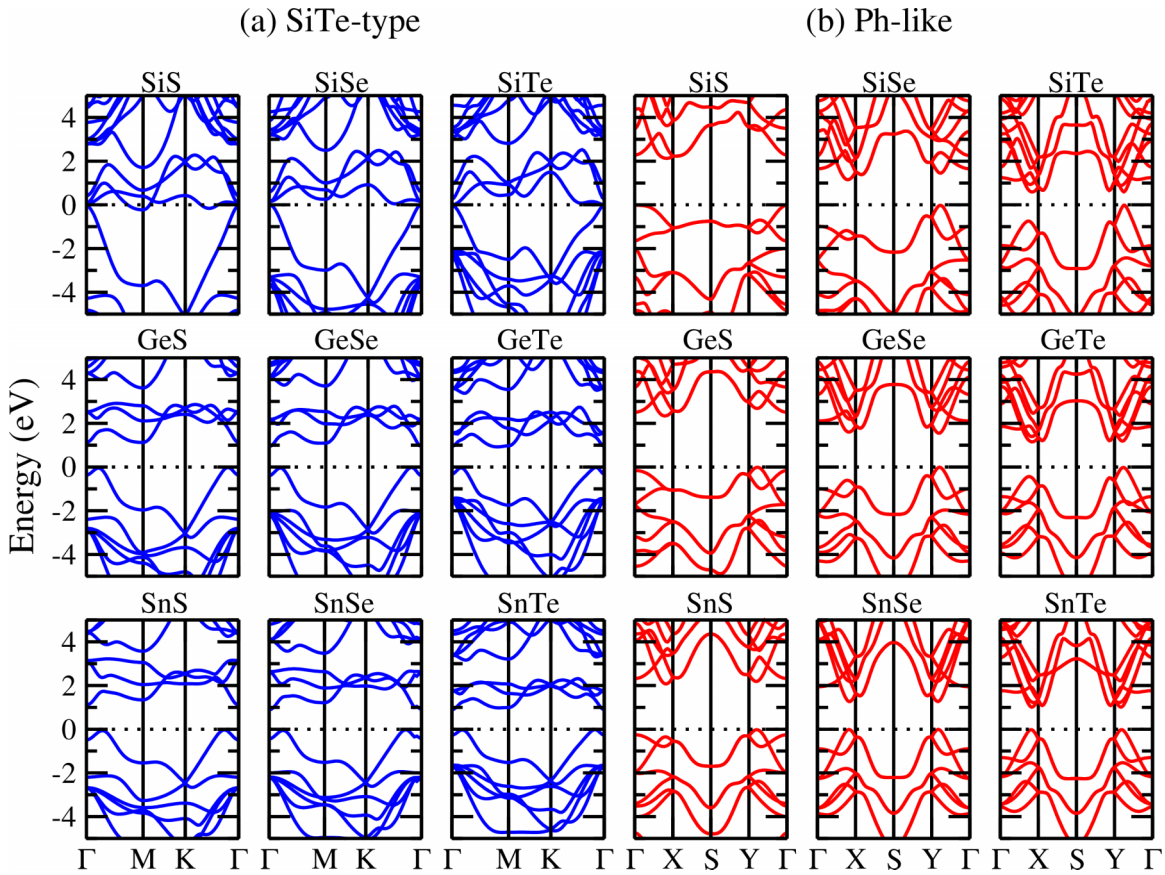

FIG. 5. Electronic band structures calculated with the HSE06 hybrid functional for group-IV monochalcogenides in (a) the SiTe-type and (b) Ph-like structures. The dotted lines indicate the Fermi level, set to zero for all materials.

strong optical-phonon scattering [55]. Moreover, a change in the chalcogen species (S → Se → Te) lowers the maximum frequency, and the same behavior is observed by changing the group-IV element (Si → Ge → Te). We attribute this result to lowering the vibration frequencies resulting from longer (weaker) M-Q bond lengths [56].

Focusing first on SiTe-type compounds, we note that all phonon frequencies are real (nonimaginary), indicative of dynamical stability in the freestanding morphology as in Fig. 4(a).

When we analyze the Ph-like compounds, our results show that all compositions have imaginary frequencies, as seen in Fig. 4(b). However, their behaviors can be separated into three groups: (i) the imaginary frequency of the valleys being small ($|\omega| \leqslant 0.30$ THz) is considered stable [44], e.g., in SiTe, GeTe, SnS, and SnSe; (ii) the imaginary frequency being up to 10% of the highest frequency is considered semistable [57], e.g., in SiS, SiSe, GeS, and GeSe; and (iii) compounds that do not fit any of the previously mention criteria are considered unstable in freestanding form, although they can be stabilized when synthesized on a substrate or under different strain conditions [53,58,59], e.g., SnTe.

C. Electronic and optical properties

1. Electronic properties

Considering the general stability of all SiTe-type compounds from the phonon calculations and that a few compounds in the Ph-like structure have imaginary frequencies on a level that can be considered stable [44] or stable when deposited on a substrate [53], we therefore discuss the electronic and optical properties for all the compounds and address the differences between the two structures.

In order to analyze the electronic properties, we calculated electronic band structures with the hybrid HSE06 functional, which provides a better description of band gaps and band dispersions than the semilocal PBE due to partial correction of self-interaction errors. Tests including spin-orbit coupling (SOC) were performed using the HSE06 functional. However, when SOC effects were evaluated, their values were not relevant as the splittings in the conduction and valence bands were small (these results can be seen in the Supplemental Material [38]), apart from the already known SiTe-type compound SiTe turning into a topological insulator [60].

The band structures for all materials in the SiTe-type phase have similar characteristics, as shown in Fig. 5(a). SiS, SiSe, and SiTe have band gaps of 0.00, 0.06, and 0.00 eV, respectively. The remaining materials have indirect band gaps in the range of 0.91 to 1.14 eV with similar band lines; that is, the valence-band maximum (VBM) is along the Γ-M path, while the conduction-band minimum (CBM) is at the Γ point. Furthermore, all valence bands have wide dispersions (valence bandwidth larger than 5 eV), while the conduction bands are much flatter, especially around the high-symmetry K point. These localized states give rise to peaks in optical spectra, as in absorption coefficients and refractive indexes.

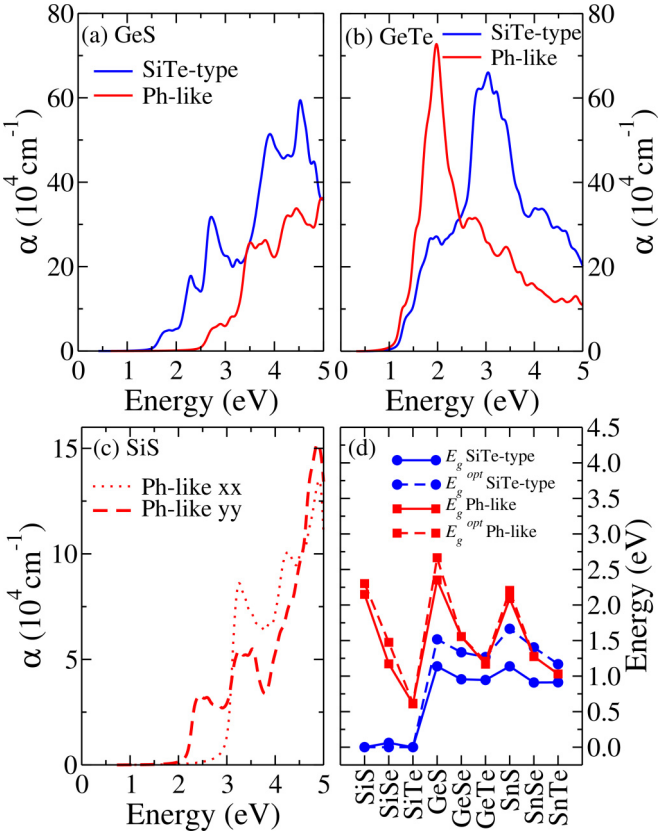

FIG. 6. Absorption coefficient α for (a) GeS and (b) GeTe in the SiTe-type and Ph-like structures. The polarization of the absorption coefficient for SiS in the Ph-like structure is shown in (c), and the fundamental optical gaps, E_g and E_g^{opt}, for all group-IV MQ compounds are shown in (d).

The band structures of the compounds in the Ph-like phase, shown in Fig. 5(b), have direct band gaps for GeSe (1.56 eV) and SnTe (1.03 eV) with the VBM and CBM in valleys along the Y-Γ direction. All other compounds have indirect band gaps in the range of 0.6 to 2.4 eV. The VBM and CBM positions vary with the material composition, being located in valleys along either Γ-X or Γ-Y. Moreover, vertical valley-valley transitions dominate excitations with energies below 4 eV. These features make these materials suitable for valleytronics, with electronic excitations modulated by light polarization [61,62].

2. *Optical properties*

The absorption coefficients and the refractive indexes were calculated through the dielectric tensor. These calculations were performed using the PBE functional with a rigid shift based on HSE06, defined as $\delta_{\text{HSE06}} = E_g^{\text{HSE06}} - E_g^{\text{PBE}}$. Figure 6(a) shows the absorption coefficient for the GeS compound, which indicates that in the visible range of the spectra the SiTe-type structures absorb more light than the Ph-like structures. However, Fig. 6(b) indicates that by changing the chalcogen species (S $\rightarrow$ Se $\rightarrow$ Te), a redshift of the absorption coefficient peaks occurs. In comparison, the Ph-like structures show overall higher light absorption in the visible. The same behavior is seen for the other elements of group-IV MQ compounds, which are included in the Supplemental Material [38]; note that results for the Si compounds in the SiTe-type structures are not included due to their metallic behavior or because the band gap is close to zero.

Anisotropic absorption coefficients in the xx and yy directions were investigated in earlier studies due to valley asymmetries in the Γ-X and Γ-Y directions [63,64]. Herein, we investigate this feature because the band structures for most our investigated Ph-like compounds present this aspect and no absorption anisotropy was observed for any of the investigated materials in the SiTe-type structures.

Although SnSe and SnTe do not present significant anisotropy, all other structures do. However, the SiS Ph-like compound displays a singular behavior considering the fact that it has the highest anisotropy among all the compounds. Figure 6(c) shows the absorption coefficient for the xx and yy directions of the SiS Ph-like compound. A higher absorption peak at lower energies is observed with yy polarization, while for higher energies the xx direction has a higher absorption coefficient. Moreover, the optical band gap value for the xx component (2.91 eV) differs from the band gap for the yy component (2.15 eV) by 0.76 eV. Considering that this structure presents high stability based on energetic and vibrational considerations, this result motivates future experimental exploration of valleytronics in SiS in the Ph-like structure.

The fundamental (E_g) and optical (E_g^{opt}) band gaps are indicated in Fig. 6(d). Both E_g and E_g^{opt} have similar values for the Ph-like compounds as a consequence of their lowest-energy VBM $\rightarrow$ CBM transitions in the valleys in the Γ-X and/or Γ-Y directions with similar energies; thus, the direct band gap is close to the fundamental one. Moreover, it is possible to note a higher dependence on the chalcogen species (S $\rightarrow$ Se $\rightarrow$ Te); for example, E_g^{opt} decreases from 2.30 eV (for SiS) to 0.62 eV (for SiTe), representing a sizable band gap reduction of 70%. The Ge- and Sn-based monochalcogenides show similar behavior.

For the SiTe-type compounds, aside from the Si compounds that display metallic behavior or have a small band gap, the E_g and E_g^{opt} values differ by at least 0.26 eV. Moreover, both E_g and E_g^{opt} tend to behave as a plateau, with their values varying by $\sim$0.2 eV, indicating much lower dependence in the chalcogen species. Also, all SiTe-type compounds have optical band gaps in the range of 0.70 to 2.1 eV, which includes the optimum value for solar absorption peak efficiency.

The complex refractive index, seen in Fig. 7, is given by $\tilde{n} = n + ik$, where n is the real part and k is the imaginary part. Considering only the real part, in Fig. 7(a), the refractive index has a peak near 500 nm, followed by a small decay that has almost no oscillations for the Ph-like structure, while for the SiTe-type structure there is a higher peak near 600 nm, followed by an oscillation and then a small decay. Meanwhile, the imaginary part of the Ph-like refractive index has a peak near 400 nm, with a subsequent monotonic decay, and the SiTe-type structure has a peak around 550 nm, with an oscillatory decay.

Figure 7(b) indicates that when the chalcogen in the Ph-like phase changes (S $\rightarrow$ Se), the peaks in the real and imaginary parts n and k tend to redshift, in addition to being more

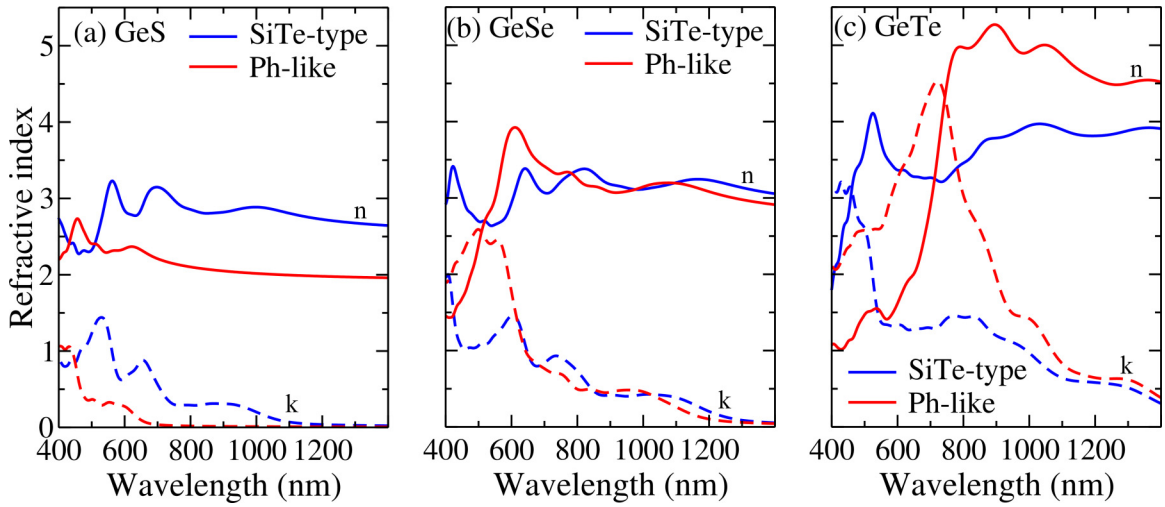

FIG. 7. Real and imaginary parts of the refractive index, n (solids lines) and k (dashed lines), for (a) GeS, (b) GeSe, and (c) GeTe in the SiTe-type and Ph-like structures.

oscillatory and increasing by almost a factor of 1.5 for the real part and 2 for the imaginary part. Meanwhile, the SiTe-type structure shows an increase on the order of 0.5 in n and 1 in k, and both peaks are blueshifted with a more oscillatory behavior. The peak increase in both the imaginary and real parts of the refractive index when changing the chalcogen from Se to Te follows the same trend as changing S $\rightarrow$ Se, with both the Ph-like and SiTe-type structures having the peaks redshifted and displaying more oscillations, as in Fig. 7(c). The other compounds display behavior similar to that described here and are included in the Supplemental Material [38]. Our results therefore indicate that the refractive index can be used to differentiate the composition and phase of the MQ materials. Li *et al.* showed both calculated n and k agreed with their experimental values in order to identify different phases of In_2Se_3 [65].

IV. BULK VERSUS MONOLAYERS: ENERGETIC STABILITY

The previously synthesized GeSe, SnSe, and SnTe were reported in the Ph-like phase [22,51,52], whereas the results reported here state that for these three compounds the most stable phase would be the SiTe-type one. To better understand the polymorphism of these compounds [66] bulk structures comprising two monolayers in their unit cells were calculated while considering the AA and AB stacking patterns for the SiTe-type phase and the previously considered synthesized AA stacking for the Ph-like phase [67] (results are given in the Supplemental Material [38]). This section contrasts formation energies, the decomposition of energies, and charge density for the lowest-energy bulk structures with their monolayer counterparts.

Figure 8 depicts the formation enthalpy for the monolayers previously discussed in Sec. III B 1 and their bulk forms. The monolayers have a more stable phase for the SiTe-type structures, with the SnSe compound possessing similar enthalpy values for both phases. When the same analysis is carried out for the bulk structures, the behavior is the opposite. The most stable phase becomes the Ph-like one, with the GeSe compound having similar values. It is also worth mentioning that the monolayers present lower values of formation enthalpy than the bulk ones, indicating a higher energetic stability, which motivates the experimental synthesis of these materials in their freestanding form. Moreover, both forms follow the same trend as GeSe in having a high enthalpy value followed by an enthalpy decrease for SnSe but an increasing value for SnTe.

In this work, the decomposition of energetic properties [68] was used as a tool to better understand the interlayer interactions. Table II shows the exfoliation energy for the monolayers frozen in their bulk geometries, $E_{\rm exf}^{\rm frozen} = (E_{\rm tot}^{\rm bulk} - E_{1L}^{\rm frozen} - E_{2L}^{\rm frozen})/2A$, where $E_{\rm tot}^{\rm bulk}$, $E_{1L}^{\rm frozen}$, $E_{2L}^{\rm frozen}$, and $2A$ are the total energy of the bulk, the energy of frozen layer 1, the energy of frozen layer 2, and the number of interfaces (2) times the area of the interfacial surface, respectively; the exfoliation energy for the fully optimized monolayers,

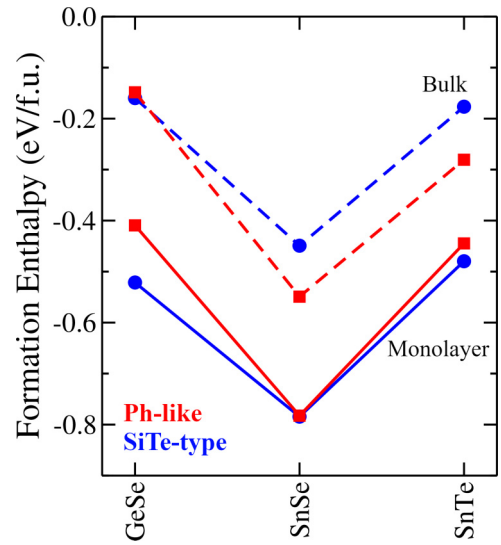

FIG. 8. Calculated formation enthalpies for group-IV monochalcogenides in the SiTe-type and Ph-like structures in monolayer (solid lines) and bulk (dashed lines) forms.

TABLE II. Energetic properties of SiTe-type and Ph-like bulks: exfoliation energy for the layers frozen in their bulk geometries $E_{\text{exf}}^{\text{frozen}}$, exfoliation energy for the fully optimized monolayers $E_{\text{exf}}^{\text{free}}$, and average deformation energy $\overline{E_{\text{def}}}$.

MQ	Phase	$E_{\text{exf}}^{\text{frozen}}$ ($\frac{\text{meV}}{\text{Å}^2}$)	$E_{\text{exf}}^{\text{free}}$ ($\frac{\text{meV}}{\text{Å}^2}$)	$\overline{E_{\text{def}}}$ ($\frac{\text{meV}}{\text{Å}^2}$)
GeSe	SiTe-type	16.80	16.74	0.06
	Ph-like	36.17	28.74	7.43
SnSe	SiTe-type	16.41	16.35	0.06
	Ph-like	42.60	27.77	14.82
SnTe	SiTe-type	17.35	17.24	0.11
	Ph-like	42.99	32.23	10.76

$E_{\text{exf}}^{\text{free}} = (E_{\text{tot}}^{\text{bulk}} - E_{1L}^{\text{relaxed}} - E_{2L}^{\text{relaxed}})/2A$, where E_{1L}^{relaxed} and E_{2L}^{relaxed} represent the energy of the fully optimized layer 1 and the fully optimized layer 2; and the average deformation energy for monolayers, $\overline{E_{\text{def}}} = (E_{\text{def}}^1 + E_{\text{def}}^2)/2$, where $E_{\text{def}}^1 = E_{1L}^{\text{frozen}} - E_{1L}^{\text{relaxed}}$ and $E_{\text{def}}^2 = E_{2L}^{\text{frozen}} - E_{2L}^{\text{relaxed}}$.

SiTe-type structures present the lowest $E_{\text{exf}}^{\text{frozen}}$, with values of 16.80, 16.41, and 17.35 meV/Å^2 for GeSe, SnSe, and SnTe, respectively. The values obtained for the Ph-like structures are 36.17, 42.60, and 42.99 meV/Å^2 for the same compounds, representing about double the values of the SiTe-type structures. $E_{\text{exf}}^{\text{frozen}}$ for the Ph-like phase approaches 40 meV/Å^2, which is twice the typical van der Waals binding exfoliation energies [69,70], indicating the presence of another interlayer binding mechanism besides van der Waals interactions for this phase. $E_{\text{exf}}^{\text{free}}$ also presents higher energy values for the Ph-like structures than for the SiTe-type. The energies are 28.74, 27.77, and 32.23 meV/Å^2 for Ph-like structures, versus 16.74, 16.35, and 17.24 meV/Å^2 for SiTe-type structures with GeSe, SnSe, and SnTe compositions, respectively. The fact that SiTe-type structures possess similar values for both exfoliation energies means that their monolayer deformation energies are low, in the range of 0.06 to 0.11 meV/Å^2, which means that the interlayer interaction do not affect the monolayer geometries in the bulks. In contrast, $\overline{E_{\text{def}}}$ for the Ph-like structures falls in the range of 7.43 to 14.82 meV/Å^2, values two orders of magnitude higher than those of the other phase, showing that the layers cause a considerable deformation in each other in this phase.

We further characterize the interlayer binding mechanisms via spatially resolved charge density analysis for both phases. The slice of the charge density of the GeSe compounds is shown in Fig. 9 (other compounds are shown in the Supplemental Material [38]). There is a concentration of charge in the interlayer region only for the Ph-like structure; nevertheless, the SiTe-type phase presents a minimum charge in the interlayer region, typical of pure van der Waals bounds. These results corroborate the energy values shown in Table II.

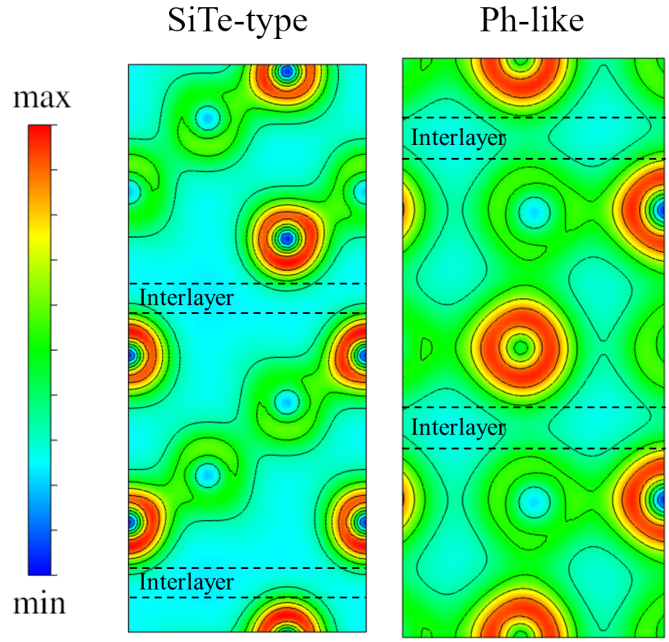

FIG. 9. Slice of the charge density for the GeSe compound for the SiTe-type (left) and Ph-like (right) structures.

V. CONCLUSIONS

We carried out DFT-PBE/HSE06 calculations to investigate the structural and optoelectronic properties of the family of monochalcogenides MQ, where M = Si, Ge, and Sn and Q = S, Se, and Te, in the $P\bar{3}m1$ (SiTe-type) and $Pmn2_1$ (Ph-like) structures. The lattice parameters of the hexagonal SiTe-type structures increase monotonically as a function of the atomic radii. On the other hand, in the orthorhombic Ph-like structures, only a_0 behaves in the same way, while b_0 shows nonmonotonic behavior. This is because the angular variation tends to reduce b_0, while atomic radii tend to increase it, resulting in higher anisotropy parameters (b_0/a_0) for lighter compounds and a tendency to approach 1 for Te-based materials.

The calculated formation enthalpies show that, except for the SnS compound, the SiTe-type phases are overall the lowest-energy structures despite being the least investigated. Most of the MQ materials synthesized so far were reported in the Ph-like structure [22,51,52]. The calculated phonon spectra show that all SiTe-type materials are structurally stable, i.e., do not have imaginary frequencies. The materials in the Ph-like structure were divided into three groups, namely, (i) stable (SiTe, GeTe, and SnS), (ii) semistable (SiS, SiSe, GeS, and GeSe) and (iii) unstable (SnSe and SnTe), according to the absolute value of the negative frequencies at Γ. These negative frequencies near Γ may indicate structural lattice instabilities but cannot rule out that these materials may be stabilized when deposited on a substrate, when under strain, or as higher-temperature phases.

For the electronic properties, all SiTe-type compounds have indirect band gaps in the range from 0.9 to 1.1 eV, with wide dispersions in the valence band, except Si-based compounds, which present band gaps narrower than 0.06 eV. In the Ph-like structure, GeSe and SnTe have direct band gaps of 1.56 and 1.03 eV, respectively; meanwhile, the other compounds have an indirect band gap in the range from 0.61 to 2.35 eV. The VBM and CBM are located along either the Γ-X or Γ-Y valley, making these materials promising for valleytronics. Due to its high anisotropy, the Ph-like SiS

compound presents an interesting polarization in the absorption coefficient, with an E_g^{opt} difference between the *xx* and *yy* directions of 0.76 eV.

For both phases, the gap is smaller for chalcogen species with larger atomic radii (S → Se → Te). This redshift is also observed for the absorption coefficient in both phases, being more significant in the Ph-like phase than in the SiTe-type phase. The fundamental and optical band gaps, E_g and E_g^{opt}, for the SiTe-type phase show small variations and are in the range of 0.9 to 1.7 eV; that is, they fall in the range of the solar absorption peak efficiency, while Ph-like compounds have gaps outside this range. The complex refractive index of the two phases shows distinct behavior, with peaks characteristic of each structure. For this reason, we propose here the use of this parameter to differentiate and identify the phases with a given composition.

The comparison of the energetic properties between the bulks and the monolayers showed an inversion of the stability of the SiTe-type and Ph-like phases, with the Ph-like phase being more energetically stable than the SiTe-type phase for SnSe and SnTe, while the GeSe compounds had close formation enthalpies. However, the monolayers still present lower formation energies than the bulks, indicating a higher stability. The exfoliation energy for the frozen bulk geometries shows values around double those for the Ph-like structures, reaching twice the typical van der Waals exfoliation energies, 40 meV/Å^2, while the exfoliation energy for the fully optimized monolayers presents a reduction in the Ph-like structures energies while still being higher than in the SiTe-type structures, indicating a deformation of the monolayer geometries. This deformation has a range from 0.06 to 0.11 meV/Å^2 for the SiTe-type structures that represents a small interlayer interaction, while the range of the Ph-like structure goes from 7.43 to 14.82 meV/Å^2, which represents considerable deformation of the layers caused by their interaction. The slice of the charge density showed a concentration of charge in the interlayer region of the Ph-like compounds and minimum charge in the interlayer of the SiTe-type compounds. Last, we hope these results will attract attention to the dependence of the electronic and optical properties on the crystal structure in this family of group-IV monochalcogenide materials, motivating further theoretical and experimental studies.

ACKNOWLEDGMENTS

The authors gratefully acknowledge support from FAPESP (São Paulo Research Foundation) and Shell, Grants No. 2017/11631-2 and No. 2018/21401-7, and the strategic importance of the support given by ANP (Brazil's National Oil, Natural Gas and Biofuels Agency) through the R&D levy regulation. M.B.P.Q. and J.M.B. gratefully acknowledge the Coordenação de Aperfeiçoamento de Pessoal de Nível Superior – Brasil (CAPES), Finance Code 001, for granting scholarships. M.P.L. gratefully acknowledges financial support from CNPq (Brazilian National Council for Scientific and Technological Development) Grant No. 308752/2020-1. The authors are thankful for the infrastructure provided to our computer cluster by the Department of Information Technology, Campus São Carlos. A.J. acknowledges support from the National Science Foundation, Award No. #OIA-2217786, and the use of Bridges-2 at PSC through allocation DMR150099 from the Advanced Cyberinfrastructure Coordination Ecosystem: Services & Support (ACCESS) program, which is supported by National Science Foundation Grants No. 2138259, No. 2138286, No. 2138307, No. 2137603, and No. 2138296. This research was supported in part through the use of DARWIN computing system DARWIN – A Resource for Computational and Data-intensive Research at the University of Delaware and in the Delaware Region, R. Eigenmann, B. E. Bagozzi, A. Jayaraman, W. Totten, and C. H. Wu, University of Delaware, 2021 [71].

[1] W. Shen, C. Hu, J. Tao, J. Liu, S. Fan, Y. Wei, C. An, J. Chen, S. Wu, Y. Li, J. Liu, D. Zhang, L. Sun, and X. Hu, Resolving the optical anisotropy of low-symmetry 2D materials, Nanoscale **10**, 8329 (2018).

[2] C. Wang, G. Zhang, S. Huang, Y. Xie, and H. Yan, The optical properties and plasmonics of anisotropic 2D materials, Adv. Optical Mater. **8**, 1900996 (2020).

[3] A. R. Brill, E. Koren, and G. de Ruiter, Molecular functionalization of 2D materials: From atomically planar 2D architectures to off-plane 3D functional materials, J. Mater. Chem. C **9**, 11569 (2021).

[4] K. S. Novoselov, A. K. Geim, S. V. Morozov, D. Jiang, Y. Zhang, S. V. Dubonos, I. V. Grigorieva, and A. A. Firsov, Electric field effect in atomically thin carbon films, Science **306**, 666 (2004).

[5] K. S. Novoselov, Nobel lecture: Graphene: Materials in the flatland, Rev. Mod. Phys. **83**, 837 (2011).

[6] S. Haastrup, M. Strange, M. Pandey, T. Deilmann, P. S. Schmidt, N. F. Hinsche, M. N. Gjerding, D. Torelli, P. M. Larsen, A. C. Riis-Jensen, J. Gath, K. W. Jacobsen, J. J. Mortensen, T. Olsen, and K. S. Thygesen, The computational 2D materials database: High-throughput modeling and discovery of atomically thin crystals, 2D Mater. **5**, 042002 (2018).

[7] M. N. Gjerding, A. Taghizadeh, A. Rasmussen, S. Ali, F. Bertoldo, T. Deilmann, N. R. Knøsgaard, M. Kruse, A. H. Larsen, S. Manti, T. G. Pedersen, U. Petralanda, T. Skovhus, M. K. Svendsen, J. J. Mortensen, T. Olsen, and K. S. Thygesen, Recent progress of the computational 2D materials database (C2DB), 2D Mater. **8**, 044002 (2021).

[8] W. Li, X. Qian, and J. Li, Phase transitions in 2D materials, Nat. Rev. Mater. **6**, 829 (2021).

[9] F. R. Fan, R. Wang, H. Zhang, and W. Wu, Emerging beyond-graphene elemental 2D materials for energy and catalysis applications, Chem. Soc. Rev. **50**, 10983 (2021).

[10] B. Luo, G. Liu, and L. Wang, Recent advances in 2D materials for photocatalysis, Nanoscale **8**, 6904 (2016).

[11] H. Tao, Y. Gao, N. Talreja, F. Guo, J. Texter, C. Yan, and Z. Sun, Two-dimensional nanosheets for electrocatalysis in energy generation and conversion, J. Mater. Chem. A **5**, 7257 (2017).

[12] U. Krishnan, M. Kaur, K. Singh, M. Kumar, and A. Kumar, A synoptic review of MoS_2: Synthesis to applications, Superlattices Microstruct. **128**, 274 (2019).

[13] N. A. M. S. Caturello, R. Besse, A. C. H. Da Silva, D. Guedes-Sobrinho, M. P. Lima, and J. L. F. Da Silva, *Ab initio* investigation of atomistic insights into the nanoflake formation of transition-metal dichalcogenides: The examples of MoS_2, $MoSe_2$, and $MoTe_2$, J. Phys. Chem. C **122**, 27059 (2018).

[14] A. C. H. Da Silva, N. A. M. S. Caturello, R. Besse, M. P. Lima, and J. L. F. Da Silva, Edge, size, and shape effects on WS_2, WSe_2, and WTe_2 nanoflake stability: Design principles from an *ab initio* investigation, Phys. Chem. Chem. Phys. **21**, 23076 (2019).

[15] R. Besse, M. P. Lima, and J. L. F. Da Silva, First-principles exploration of two-dimensional transition metal dichalcogenides based on Fe, Co, Ni, and Cu groups and their van der Waals heterostructures, ACS Appl. Energy Mater. **2**, 8491 (2019).

[16] J. Zhou, J. Lin, X. Huang, Y. Zhou, Y. Chen, J. Xia, H. Wang, Y. Xie, H. Yu, J. Lei *et al.*, A library of atomically thin metal chalcogenides, Nature (London) **556**, 355 (2018).

[17] A. A. Soluyanov, D. Gresch, Z. Wang, Q. Wu, M. Troyer, X. Dai, and B. A. Bernevig, Type-II Weyl semimetals, Nature (London) **527**, 495 (2015).

[18] D. Akinwande, N. Petrone, and J. Hone, Two-dimensional flexible nanoelectronics, Nat. Commun. **5**, 5678 (2014).

[19] S. Das, D. Pandey, J. Thomas, and T. Roy, The role of graphene and other 2D materials in solar photovoltaics, Adv. Mater. **31**, 1802722 (2019).

[20] X. Ge, Z. Xia, and S. Guo, Recent advances on black phosphorus for biomedicine and biosensing, Adv. Funct. Mater. **29**, 1900318 (2019).

[21] Z. Hu, Y. Ding, X. Hu, W. Zhou, X. Yu, and S. Zhang, Recent progress in 2D group IV–IV monochalcogenides: Synthesis, properties and applications, Nanotechnology **30**, 252001 (2019).

[22] K. Chang and S. S. P. Parkin, Experimental formation of monolayer group-IV monochalcogenides, J. Appl. Phys. **127**, 220902 (2020).

[23] F. Xia, H. Wang, J. C. M. Hwang, A. H. C. Neto, and L. Yang, Black phosphorus and its isoelectronic materials, Nat. Rev. Phys. **1**, 306 (2019).

[24] L. C. Gomes and A. Carvalho, Electronic and optical properties of low-dimensional group-IV monochalcogenides, J. Appl. Phys. **128**, 121101 (2020).

[25] S. Barraza-Lopez, B. M. Fregoso, J. W. Villanova, S. S. P. Parkin, and K. Chang, Colloquium: Physical properties of group-IV monochalcogenide monolayers, Rev. Mod. Phys. **93**, 011001 (2021).

[26] R.-W. Zhang, C.-W. Zhang, W.-X. Ji, P. Li, P.-J. Wang, S.-S. Li, and S.-S. Yan, Silicon-based chalcogenide: Unexpected quantum spin Hall insulator with sizable band gap, Appl. Phys. Lett. **109**, 182109 (2016).

[27] M. P. Lima, R. Besse, and J. L. F. D. Silva, *Ab initio* investigation of topological phase transitions induced by pressure in trilayer van der Waals structures: The example of *h*-BN/SnTe/*h*-BN, J. Phys.: Condens. Matter **33**, 025003 (2021).

[28] Z.-Y. Li, M.-Y. Liu, Y. Huang, Q.-Y. Chen, C. Cao, and Y. He, Tuning the electronic properties of bilayer group-IV monochalcogenides by stacking order, strain and an electric field: A computational study, Phys. Chem. Chem. Phys. **20**, 214 (2018).

[29] Y. Saito, J. Tominaga, P. Fons, A. V. Kolobov, and T. Nakano, *Ab-initio* calculations and structural studies of $(SiTe)_2(Sb_2Te_3)_n$ (n: 1, 2, 4 and 6) phase-change superlattice films, Phys. Status Solidi RRL **8**, 302 (2014).

[30] P. Hohenberg and W. Kohn, Inhomogeneous electron gas, Phys. Rev. **136**, B864 (1964).

[31] W. Kohn and L. J. Sham, Self-consistent equations including exchange and correlation effects, Phys. Rev. **140**, A1133 (1965).

[32] J. Hafner, *Ab-initio* simulations of materials using VASP: Density-functional theory and beyond, J. Comput. Chem. **29**, 2044 (2008).

[33] P. E. Blöchl, Projector augmented-wave method, Phys. Rev. B **50**, 17953 (1994).

[34] J. P. Perdew, K. Burke, and M. Ernzerhof, Generalized Gradient Approximation Made Simple, Phys. Rev. Lett. **77**, 3865 (1996).

[35] J. Heyd, G. E. Scuseria, and M. Ernzerhof, Hybrid functionals based on a screened Coulomb potential, J. Chem. Phys. **118**, 8207 (2003).

[36] M. Gajdoš, K. Hummer, G. Kresse, J. Furthmüller, and F. Bechstedt, Linear optical properties in the projector-augmented wave methodology, Phys. Rev. B **73**, 045112 (2006).

[37] A. C. Dias, H. Bragança, M. P. Lima, and J. L. F. Da Silva, First-principles investigation of the role of Cr in the electronic properties of the two-dimensional $Mo_xCr_{1-x}Se_2$ and $W_xCr_{1-x}Se_2$ alloys, Phys. Rev. Mater. **6**, 054001 (2022).

[38] See Supplemental Material at http://link.aps.org/supplemental/10.1103/PhysRevB.108.085409 for additional technical details and the results of spin-orbit coupling effects, the absorption coefficient, and the refractive index and a contrasting analysis of bulks and monolayers.

[39] A. Togo and I. Tanaka, First principles phonon calculations in materials science, Scr. Mater. **108**, 1 (2015).

[40] A. Togo, First-principles phonon calculations with phonopy and phono3py, J. Phys. Soc. Jpn. **92**, 012001 (2023).

[41] V. Wang, N. Xu, J.-C. Liu, G. Tang, and W.-T. Geng, VASPKIT: A user-friendly interface facilitating high-throughput computing and analysis using VASP code, Comput. Phys. Commun. **267**, 108033 (2021).

[42] M. P. Lima, A. Fazzio, and A. J. R. da Silva, Interfaces between buckling phases in silicene: *Ab initio* density functional theory calculations, Phys. Rev. B **88**, 235413 (2013).

[43] L. Wang, A. Kutana, X. Zou, and B. I. Yakobson, Electro-mechanical anisotropy of phosphorene, Nanoscale **7**, 9746 (2015).

[44] L. Seixas, Janus two-dimensional materials based on group IV monochalcogenides, J. Appl. Phys. **128**, 045115 (2020).

[45] M. S. Alam, V. Dremov, P. Müller, A. V. Postnikov, S. S. Mal, F. Hussain, and U. Kortz, STM/STS observation of polyoxoanions on HOPG surfaces: The wheel-shaped $[Cu_{20}Cl(OH)_{24}(H_2O)_{12}(P_8W_{48}O_{184})]^{25-}$ and the ball-shaped $[\{Sn(Ch_3)_2(H_2O)\}_{24}\{Sn(Ch_3)_2\}_{12}(A-PW_9O_{34})_{12}]^{36-}$, Inorg. Chem. **45**, 2866 (2006).

[46] R. D. Shannon, Revised effective ionic radii and systematic studies of interatomic distances in halides and chalcogenides, Acta Crystallogr., Sect. A **32**, 751 (1976).

[47] B. Sa, Z. Sun, and B. Wu, The development of two dimensional group IV chalcogenides, blocks for van der Waals heterostructures, Nanoscale **8**, 1169 (2016).

[48] X. Lv, W. Wei, Q. Sun, F. Li, B. Huang, and Y. Dai, Two-dimensional germanium monochalcogenides for photocatalytic water splitting with high carrier mobility, Appl. Catal., B **217**, 275 (2017).

[49] L. C. Gomes and A. Carvalho, Phosphorene analogues: Isoelectronic two-dimensional group-IV monochalcogenides with orthorhombic structure, Phys. Rev. B **92**, 085406 (2015).

[50] Y. Pan and E. Yu, First-principles investigation of structural stability, mechanical and thermodynamic properties of Pt_3Zr_5 compounds, Phys. B (Amsterdam, Neth.) **611**, 412936 (2021).

[51] D. D. I. Vaughn, R. J. Patel, M. A. Hickner, and R. E. Schaak, Single-crystal colloidal nanosheets of GeS and GeSe, J. Am. Chem. Soc. **132**, 15170 (2010).

[52] L. Li, Z. Chen, Y. Hu, X. Wang, T. Zhang, W. Chen, and Q. Wang, Single-layer single-crystalline SnSe nanosheets, J. Am. Chem. Soc. **135**, 1213 (2013).

[53] A. Banik, T. Ghosh, R. Arora, M. Dutta, J. Pandey, S. Acharya, A. Soni, U. V. Waghmare, and K. Biswas, Engineering ferroelectric instability to achieve ultralow thermal conductivity and high thermoelectric performance in $Sn_{1-x}Ge_xTe$, Energy Environ. Sci. **12**, 589 (2019).

[54] S. R. Jai Likith and C. V. Ciobanu, Structure and stability of van der Waals layered group-IV monochalcogenides, J. Vac. Sci. Technol. A **40**, 052202 (2022).

[55] W. Li, J. Carrete, G. K. H. Madsen, and N. Mingo, Influence of the optical-acoustic phonon hybridization on phonon scattering and thermal conductivity, Phys. Rev. B **93**, 205203 (2016).

[56] N. Y. Dzade, K. O. Obodo, S. K. Adjokatse, A. C. Ashu, E. Amankwah, C. D. Atiso, A. A. Bello, E. Igumbor, S. B. Nzabarinda, J. T. Obodo, A. O. Ogbuu, O. E. Femi, J. O. Udeigwe, and U. V. Waghmare, Silicene and transition metal based materials: Prediction of a two-dimensional piezomagnet, J. Phys.: Condens. Matter **22**, 375502 (2010).

[57] G. K. Inui, J. F. R. V. Silveira, A. C. Dias, R. Besse, and J. L. F. D. Silva, *Ab initio* screening of two-dimensional CuQ_x and AgQ_x chalcogenides, J. Phys.: Condens. Matter **34**, 305703 (2022).

[58] M. J. Wei, W. J. Lu, R. C. Xiao, H. Y. Lv, P. Tong, W. H. Song, and Y. P. Sun, Manipulating charge density wave order in monolayer $1T$-$TiSe_2$ by strain and charge doping: A first-principles investigation, Phys. Rev. B **96**, 165404 (2017).

[59] R. Bianco, I. Errea, L. Monacelli, M. Calandra, and F. Mauri, Quantum enhancement of charge density wave in NbS_2 in the two-dimensional limit, Nano Lett. **19**, 3098 (2019).

[60] Y. Ma, L. Kou, Y. Dai, and T. Heine, Proposed two-dimensional topological insulator in SiTe, Phys. Rev. B **94**, 201104(R) (2016).

[61] J. R. Schaibley, H. Yu, G. Clark, P. Rivera, J. S. Ross, K. L. Seyler, W. Yao, and X. Xu, Valleytronics in 2D materials, Nat. Rev. Mater. **1**, 16055 (2016).

[62] A. S. Sarkar and E. Stratakis, Recent advances in 2D metal monochalcogenides, Adv. Sci. **7**, 2001655 (2020).

[63] L. Xu, M. Yang, S. J. Wang, and Y. P. Feng, Electronic and optical properties of the monolayer group-IV monochalcogenides MX (M = Ge, Sn; X = S, Se, Te), Phys. Rev. B **95**, 235434 (2017).

[64] T. Hu, C. Xu, A. Zhang, and P. Yu, Prediction of new phase 2D C_{2h} group III monochalcogenides with direct bandgaps and highly anisotropic carrier mobilities, Mater. Adv. **3**, 2213 (2022).

[65] T. Li, Y. Wang, W. Li, D. Mao, C. J. Benmore, I. Evangelista, H. Xing, Q. Li, F. Wang, G. Sivaraman, A. Janotti, S. Law, and T. Gu, Structural phase transitions between layered indium selenide for integrated photonic memory, Adv. Mater. **34**, 2108261 (2022).

[66] H. Guo, Q. Xu, X. Xuan, W. Guo, and Z. Zhang, Curvature-induced phase transitions in two-dimensional polymorphic materials, Extreme Mech. Lett. **61**, 102020 (2023).

[67] B. Mukherjee, Y. Cai, H. R. Tan, Y. P. Feng, E. S. Tok, and C. H. Sow, NIR Schottky photodetectors based on individual single-crystalline GeSe nanosheet, ACS Appl. Mater. Interfaces **5**, 9594 (2013).

[68] M. P. Lima, N. A. Caturello, and J. L. Da Silva, *Ab initio* investigation of the interface between Mo10S24 nanoflakes and the Au(111) surface: Interplay between interaction energy and morphology, Appl. Surf. Sci. **604**, 154413 (2022).

[69] T. Björkman, A. Gulans, A. V. Krasheninnikov, and R. M. Nieminen, van der Waals Bonding in Layered Compounds from Advanced Density-Functional First-Principles Calculations, Phys. Rev. Lett. **108**, 235502 (2012).

[70] J. Liao, B. Sa, J. Zhou, R. Ahuja, and Z. Sun, Design of high-efficiency visible-light photocatalysts for water splitting: MoS_2/AlN(GaN) heterostructures, J. Phys. Chem. C **118**, 17594 (2014).

[71] https://udspace.udel.edu/handle/19716/29071.